A structural study from neutron diffraction data and magnetic properties of $RMn_2O_5$ (R = La, rare earth)



1997 J. Phys.: Condens. Matter 9 8515

(http://iopscience.iop.org/0953-8984/9/40/017)

J. Phys.: Condens. Matter **9** (1997) 8515–8526. Printed in the UK PII: S0953-8984(97)83483-2

# A structural study from neutron diffraction data and magnetic properties of $RMn_2O_5$ (R = La, rare earth)

J A Alonso†, M T Casais†, M J Martínez-Lope†, J L Martínez† and M T Fernández-Díaz‡

† Instituto de Ciencia de Materiales de Madrid, CSIC, Cantoblanco, E-28049 Madrid, Spain
‡ Institut Laue Langevin, BP156X, F-38042 Grenoble Cédex 9, France

Received 15 April 1997, in final form 7 July 1997

**Abstract.** The title compounds (R = La, Pr, Nd, Sm, Eu, Tb, Ho, Er) have been prepared in polycrystalline form by a citrate technique and, excepting the Sm and Eu phases, structurally studied by high-resolution neutron powder diffraction. All the materials are isostructural (space group *Pbam*, $Z = 4$) and contain infinite chains of $Mn^{4+}O_6$ octahedra sharing edges, linked together by $Mn^{3+}O_5$ and $RO_8$ units. The size of the three kinds of coordination polyhedron regularly decreases as R cations become smaller. A bond-valence study allowed us to detect the presence of important tensile and compressive stresses in the crystal structure of $LaMn_2O_5$, which are progressively released along the series as the rare-earth size decreases. The magnetic properties strongly depend on the nature of R, going from the spin-glass behaviour observed at low temperature in $LaMn_2O_5$ to the field-induced transitions exhibited by $NdMn_2O_5$. A cusp in the susceptibility curves suggests an antiferromagnetic ordering at low temperatures, which is masked in the compounds containing strongly paramagnetic rare earths (Tb, Ho, Er). At high temperatures the paramagnetic moments are consistent in all cases with the presence of high-spin $Mn^{3+}$ and $Mn^{4+}$ cations.

## 1. Introduction

Very recently, the observation of large negative magnetoresistance effects in mixed-valence manganites [1] based on $LaMnO_3$ has renewed the interest in the study of manganese oxides, trying to find relationships between the structural features and the magnetic and transport properties of these materials. From this point of view, many oxides which were first described in the fifties or sixties are now being revisited, paying especial attention to the fine structural details and expanding the physical measurements.

This is the case of the $RMn_2O_5$ (R = La, Y or rare earth) family of oxides, which contain manganese in two different oxidation states, $Mn^{3+}$ and $Mn^{4+}$. The crystal structure of these materials presents the additional interest of containing infinite chains of edge-sharing $MnO_6$ octahedra parallel to the ***c*** axis, with rather short metal–metal distances along the chains, for instance Mn1–Mn1 = 2.750(2) Å in the Nd compound [2]. Important implications for the physical properties of these phases can be presumed from such short distances. The magnetic properties have not yet been described, and the structural information for the whole series is far from complete.

The $RMn_2O_5$ series was first described by Quezel-Ambrunaz *et al* [3] and Bertaut *et al* [4], who prepared single-crystal phases from a $Bi_2O_3$ flux for R = rare earth, and gave the unit-cell parameters for the complete series. The crystal structure of the isomorphic series

0953-8984/97/408515+12$19.50  

was solved for $HoMn_2O_5$ [3] and subsequently refined for other rare earths: $DyMn_2O_5$ [5], $ErMn_2O_5$ and $TbMn_2O_5$ [6] and, more recently, $NdMn_2O_5$ [2]. All these studies were performed from single-crystal data.

The structure is orthorhombic and contains $MnO_6$ and $MnO_5$ units. From considerations relating the Mn–O distances and the observed magnetic couplings, it can be assumed that octahedrally coordinated manganese cations are tetravalent, whereas $MnO_5$ square-planar pyramids correspond to $Mn^{3+}$ cations. As for the magnetic structures, they were studied for R = Nd [7], Dy [8], Tb and Er [6, 7] from neutron diffraction data; they are rather complex and show amplitude modulation of the ordered magnetic moments.

Very recently [9] the preparation and basic characterization of five polycrystalline oxides of the $RMn_2O_5$ series (R = La, Pr, Nd, Sm, Eu) was reported. The aim of the present paper is to complete this study describing the fine structural details of six members of the series (R = La, Pr, Nd, Tb, Ho, Er), from high-resolution neutron powder diffraction data, and to discuss the structural evolution along the series from bond valence considerations. The magnetic susceptibility of these materials is also given.

## 2. Experimental details

Single-phased products of composition $RMn_2O_5$ (R = La, Pr, Nd, Sm, Eu, Tb, Ho, Er) were obtained as dark-brown polycrystalline powders by a citrate technique, as described elsewhere [9]. The final materials were annealed at 1273 K either under high oxygen pressure (200 bar), for R = La, ..., Eu, or in air, for the heavier rare-earth compounds, R = Tb, Ho, Er.

X-ray powder diffraction (XRD) patterns were collected with Cu K$\alpha$ radiation in a Siemens D-501 goniometer controlled by a DACO-MP computer. Neutron powder diffraction (NPD) diagrams of $RMn_2O_5$ (R = La, Pr, Nd, Tb, Ho, Er) were collected at room temperature in the high-resolution D2B diffractometer at the ILL-Grenoble, with a wavelength of 1.594 Å, selected from a Ge monochromator. About 6 g of each sample were contained in a cylindrical vanadium can. The time consumed in each data collection was about 3 hours.

The Rietveld method [10] was used to refine the crystal structures, using the FULLPROF program [11]. The line shape of the diffraction peaks was generated by a pseudo-Voigt function, and the background refined to a fifth-degree polynomial. The coherent scattering lengths for La, Pr, Nd, Tb, Ho, Er, Mn and O were, respectively, 8.24, 4.58, 7.69, 7.38, 8.01, 7.79, −3.73 and 5.803 fm. In the final run the following parameters were refined: six background coefficients, zero-point, half-width, pseudo-Voigt and asymmetry parameters for the peak shape; scale factors, positional, thermal isotropic factors and unit-cell parameters. In the final cycle the shifts in the atomic parameters were zero up to the fourth decimal place.

Magnetic measurements were performed on a PPMS (Quantum Design) system, by the extraction method, in a temperature range from 2 to 400 K and a maximum magnetic field of 9 T. The expected sensitivity of the system is $2.5 \times 10^{-5}$ emu. Also a.c. susceptibility was measured in the same temperature range, with a modulated magnetic field of 10 Oe.

## 3. Results and discussion

### *3.1. Structural study*

Figure 1 shows the XRD patterns of $RMn_2O_5$ (R = La, Pr, Nd, Sm, Eu, Tb, Ho, Er). They all correspond to pure phases, that can be indexed in an orthorhombic unit cell, isotypic to

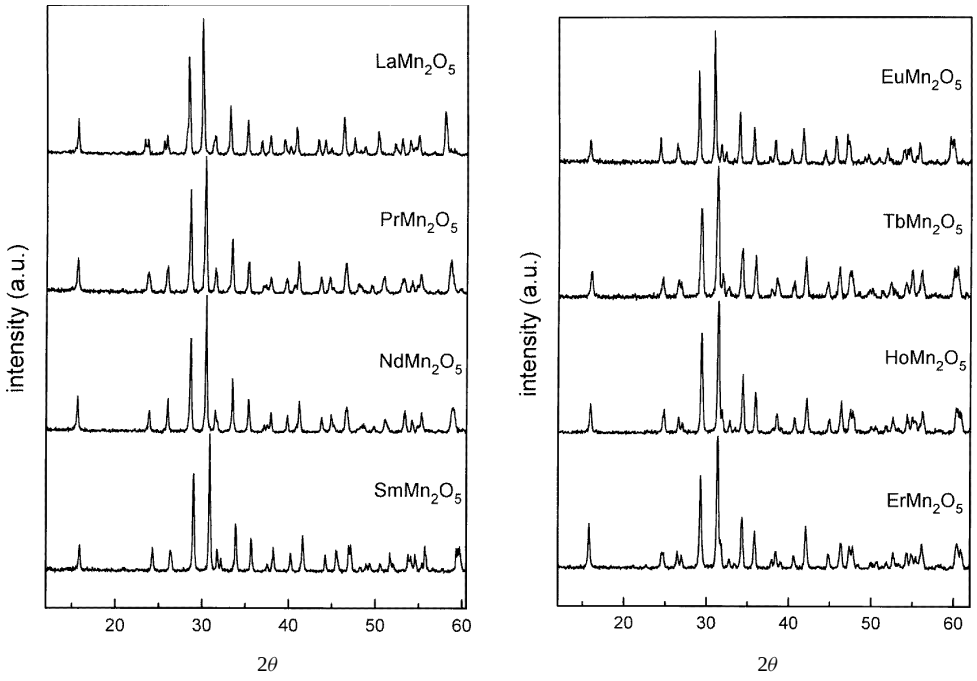


**Figure 1.** X-ray powder diffraction data for $RMn_2O_5$.

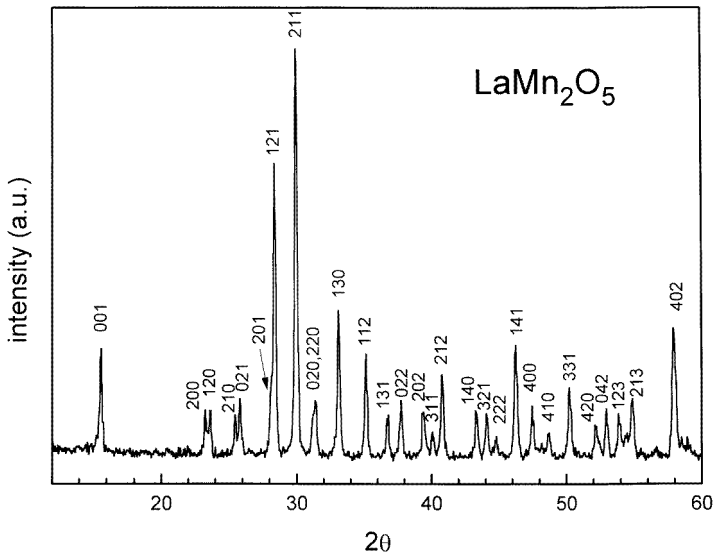


**Figure 2.** Indexing of the XRD pattern of $LaMn_2O_5$, according to an orthorhombic unit cell with dimensions $a = 7.6823(2)$, $b = 8.7056(2)$ and $c = 5.7214(1)$ Å.

$YMn_2O_5$ [12], with no additional peaks which could indicate the presence of superstructures or departure from the mentioned symmetry. Figure 2 illustrates the indexing of the XRD reflections of $LaMn_2O_5$.

The crystal structure of the six compounds with R cations non-absorbing for neutrons was studied by profile analysis of NPD data. The structural details for R = Sm, Eu, have been studied by XRD and can be found elsewhere [9]. The structures were refined taking as starting structural model that of $NdMn_2O_5$ [2], in the space group *Pbam* (No 55), $Z = 4$. The unit-cell parameters and volume are listed in table 1. They show a regular variation with the ionic radii of the rare-earth cations [13], according to the well known lanthanide contraction. An example of the good agreement between the observed and calculated profiles of the pattern is given in figure 3 for $LaMn_2O_5$.

The final atomic coordinates after the refinement are listed in table 2. Final bonding distances and angles are given in tables 3 and 4. A representation of the structure is shown

**Table 1.** Unit-cell parameters and volume for $RMn_2O_5$ determined either from NPD or XRD at room temperature.

| R | $r(R^{3+})$ (Å)[a] | $a$ (Å) | $b$ (Å) | $c$ (Å) | $V$ (Å$^3$) |
|---|---|---|---|---|---|
| La | 1.16 | 7.6823(2) | 8.7056(2) | 5.7214(1) | 382.64(3) |
| Pr | 1.126 | 7.5531(2) | 8.6400(2) | 5.7075(1) | 372.46(3) |
| Nd | 1.109 | 7.5051(2) | 8.6209(2) | 5.7022(1) | 368.93(3) |
| Sm[b] | 1.079 | 7.4332(7) | 8.5872(7) | 5.6956(5) | 363.55(9) |
| Eu[b] | 1.066 | 7.3986(8) | 8.5666(9) | 5.6925(6) | 360.8(1) |
| Tb | 1.040 | 7.3251(2) | 8.5168(2) | 5.6750(2) | 354.04(3) |
| Ho | 1.015 | 7.2643(3) | 8.4768(3) | 5.6700(2) | 349.15(3) |
| Er | 1.004 | 7.2360(2) | 8.4583(2) | 5.6655(1) | 346.75(3) |

[a] Taken from [13].
[b] Determined from XRD data.

**Table 2.** Structural parameters after the Rietveld refinement of NPD data for $RMn_2O_5$ oxides at room temperature. R and O2 atoms are at 4g $(x, y, 0)$ positions; Mn1 at 4f $(0, 1/2, z)$; Mn2 and O3 at 4h $(x, y, 1/2)$; O1 at 4e $(0, 0, z)$ and O4 at 8i $(x, y, z)$ positions.

| Atom | | La | Pr | Nd | Tb | Ho | Er |
|---|---|---|---|---|---|---|---|
| R | $x$ | 0.1451(3) | 0.1421(6) | 0.1420(4) | 0.1399(5) | 0.1367(4) | 0.1366(4) |
| | $y$ | 0.1736(3) | 0.1732(5) | 0.1724(3) | 0.1726(4) | 0.1714(4) | 0.1716(3) |
| Mn1 | $z$ | 0.2610(8) | 0.2583(10) | 0.2585(11) | 0.2618(13) | 0.2611(13) | 0.2553(11) |
| Mn2 | $x$ | 0.4114(7) | 0.4097(7) | 0.4113(8) | 0.4120(8) | 0.4126(8) | 0.4131(6) |
| | $y$ | 0.3533(5) | 0.3511(5) | 0.3527(6) | 0.3510(7) | 0.3496(7) | 0.3493(6) |
| O1 | $z$ | 0.2781(7) | 0.2780(6) | 0.2782(7) | 0.2710(9) | 0.2702(9) | 0.2711(7) |
| O2 | $x$ | 0.1525(5) | 0.1566(5) | 0.1571(6) | 0.1617(6) | 0.1637(6) | 0.1649(5) |
| | $y$ | 0.4497(4) | 0.4491(4) | 0.4469(4) | 0.4463(5) | 0.4438(5) | 0.4442(4) |
| O3 | $x$ | 0.1525(6) | 0.1511(6) | 0.1524(6) | 0.1528(7) | 0.1503(7) | 0.1501(5) |
| | $y$ | 0.4374(4) | 0.4353(4) | 0.4374(4) | 0.4324(5) | 0.4300(5) | 0.4301(4) |
| O4 | $x$ | 0.4068(2) | 0.4030(3) | 0.4009(3) | 0.3973(3) | 0.3948(3) | 0.3936(3) |
| | $y$ | 0.2061(2) | 0.2067(2) | 0.2067(3) | 0.2062(3) | 0.2063(3) | 0.2057(3) |
| | $z$ | 0.2540(5) | 0.2508(6) | 0.2515(6) | 0.2483(7) | 0.2457(6) | 0.2470(5) |
| $\chi^2$ | | 1.36 | 1.50 | 1.31 | 1.41 | 1.34 | 1.20 |
| $R_p$ | | 3.73 | 3.83 | 3.57 | 3.64 | 3.43 | 3.19 |
| $R_{wp}$ | | 4.64 | 4.78 | 4.46 | 4.51 | 4.30 | 3.99 |
| $R_{exp}$ | | 3.97 | 3.90 | 3.89 | 3.79 | 3.72 | 3.64 |
| $R_I$ (%) | | 6.22 | 6.37 | 5.29 | 7.57 | 7.54 | 4.21 |

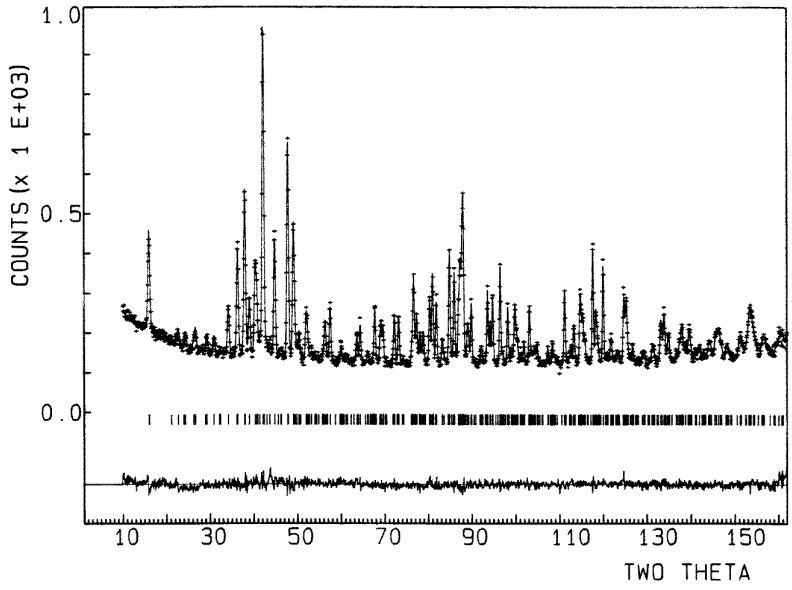


**Figure 3.** Observed (crosses), calculated (solid line) and difference (at the bottom) NPD profiles for $LaMn_2O_5$ at 295 K. The tick marks indicate the positions of the allowed Bragg reflections. For the sake of clarity only half of the experimental points are represented.

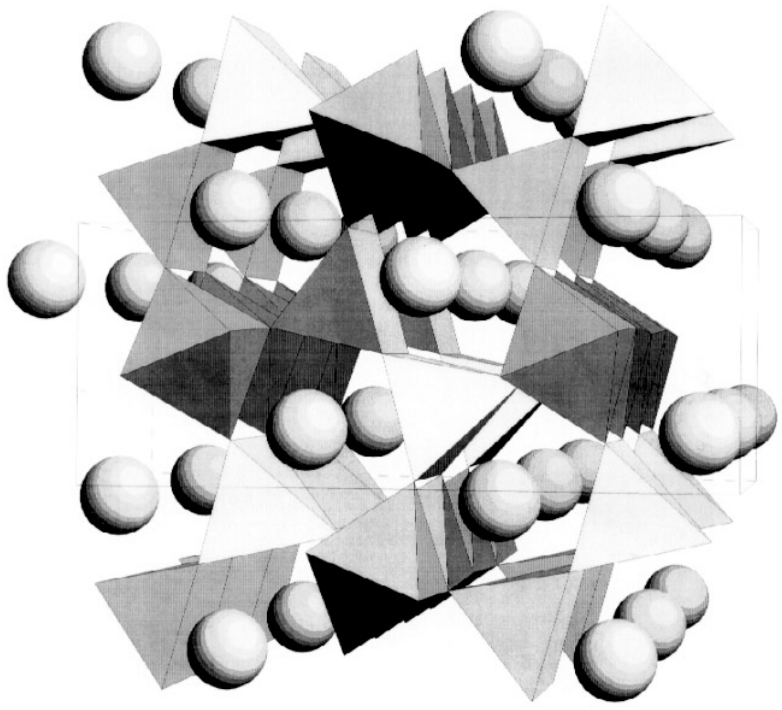

**Figure 4.** A view of the $RMn_2O_5$ structure, approximately along the ***c*** axis. Octahedra and tetragonal pyramids correspond to $Mn1O_6$ and $Mn2O_5$ units, respectively. Spheres represent R atoms.

**Table 3.** Selected interatomic distances (Å) in $RMn_2O_5$.

| | | La | Pr | Nd | Tb | Ho | Er |
|---|---|---|---|---|---|---|---|
| $Mn^{4+}O_6$ octahedra | | | | | | | |
| Mn1–O2 | (×2) | 1.948(4) | 1.941(5) | 1.942(5) | 1.954(6) | 1.958(6) | 1.933(5) |
| –O3 | (×2) | 1.881(5) | 1.875(5) | 1.870(5) | 1.847(6) | 1.838(6) | 1.858(5) |
| –O4 | (×2) | 1.932(2) | 1.931(2) | 1.931(2) | 1.912(3) | 1.910(3) | 1.903(2) |
| ⟨Mn1–O⟩ | | 1.921(2) | 1.916(2) | 1.914(2) | 1.904(2) | 1.902(2) | 1.898(2) |
| $Mn^{3+}O_5$ tetragonal pyramid | | | | | | | |
| Mn2–O1 | (×2) | 1.925(4) | 1.930(4) | 1.912(5) | 1.927(5) | 1.931(6) | 1.924(4) |
| –O3 | | 2.120(7) | 2.084(7) | 2.076(7) | 2.021(8) | 2.024(8) | 2.023(6) |
| –O4 | (×2) | 1.904(4) | 1.893(4) | 1.897(4) | 1.891(5) | 1.890(5) | 1.884(4) |
| ⟨Mn2–O⟩ | | 1.956(2) | 1.946(2) | 1.939(3) | 1.931(3) | 1.933(3) | 1.928(2) |
| $R^{3+}O_8$ bicapped prism | | | | | | | |
| R–O1 | (×2) | 2.461(3) | 2.431(4) | 2.421(3) | 2.361(4) | 2.333(4) | 2.333(3) |
| –O2 | | 2.404(4) | 2.386(5) | 2.369(4) | 2.337(5) | 2.318(5) | 2.315(4) |
| –O2 | | 2.494(4) | 2.462(4) | 2.461(5) | 2.414(5) | 2.413(5) | 2.401(4) |
| –O4 | (×2) | 2.496(3) | 2.452(4) | 2.433(3) | 2.371(4) | 2.355(4) | 2.345(3) |
| –O4 | (×2) | 2.562(3) | 2.528(4) | 2.534(3) | 2.492(4) | 2.471(4) | 2.476(3) |
| ⟨R–O⟩ | | 2.492(1) | 2.459(2) | 2.451(1) | 2.400(2) | 2.381(2) | 2.378(1) |
| Mn–Mn distances | | | | | | | |
| Mn1–Mn1 | | 2.986(7) | 2.949(8) | 2.949(9) | 2.971(10) | 2.961(10) | 2.891(9) |
| Mn1–Mn1 | | 2.735(7) | 2.759(8) | 2.734(9) | 2.704(10) | 2.709(10) | 2.774(9) |
| Mn2–Mn2 | | 2.894(7) | 2.913(7) | 2.867(7) | 2.846(8) | 2.849(9) | 2.843(7) |

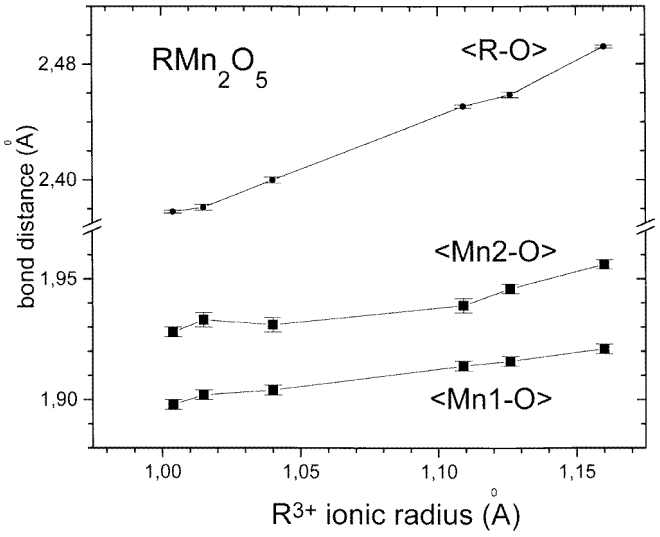


**Figure 5.** Bond-length variation with the size of R.

in figure 4. There are two different oxygen environments for Mn. Mn1 is hexacoordinated to oxygens forming $Mn1O_6$ distorted octahedra. The coordination of Mn2 is best described as slightly distorted tetragonal pyramidal. $Mn1O_6$ octahedra form infinite chains parallel to the ***c*** axis, sharing edges via O2 and O3 oxygens. The chains are interconnected by $Mn2O_5$

**Table 4.** Selected bond angles (°) for $RMn_2O_5$.

| | La | Pr | Nd | Tb | Ho | Er |
|---|---|---|---|---|---|---|
| O2–Mn1–O2 | 79.9(3) | 81.1(3) | 81.2(3) | 81.0(4) | 81.7(3) | 83.2(3) |
| O2–Mn1–O3 | 96.8(2) | 96.9(2) | 96.9(2) | 96.7(3) | 96.8(3) | 96.9(2) |
| | 175.5(3) | 175.7(3) | 176.7(3) | 175.3(4) | 175.3(4) | 175.4(3) |
| O2–Mn1–O4 | 88.3(2) | 87.8(2) | 88.2(2) | 86.9(3) | 86.9(3) | 87.4(2) |
| | 89.9(2) | 90.3(2) | 90.0(2) | 89.6(3) | 89.2(3) | 90.5(2) |
| O3–Mn1–O3 | 86.7(3) | 85.3(3) | 85.2(4) | 85.9(4) | 85.1(4) | 83.4(3) |
| O3–Mn1–O4 | 88.7(2) | 88.4(2) | 92.6(3) | 88.9(3) | 88.6(3) | 94.2(3) |
| | 93.1(2) | 93.5(2) | 89.1(3) | 94.4(3) | 95.3(3) | 87.9(2) |
| O4–Mn1–O4 | 177.6(2) | 177.5(2) | 177.6(2) | 175.4(2) | 174.8(3) | 177.2(2) |
| O1–Mn2–O1 | 82.5(3) | 82.0(2) | 82.8(3) | 84.8(4) | 85.0(4) | 84.7(3) |
| O1–Mn2–O3 | 95.9(3) | 95.7(3) | 95.3(3) | 95.1(3) | 95.0(3) | 94.8(3) |
| O1–Mn2–O4 | 88.0(2) | 87.4(2) | 87.8(2) | 86.5(2) | 86.1(3) | 86.5(2) |
| | 160.2(3) | 160.4(3) | 161.7(3) | 163.4(4) | 164.1(4) | 164.7(3) |
| O3–Mn2–O4 | 102.4(3) | 101.8(3) | 101.2(3) | 99.8(3) | 98.8(4) | 98.4(2) |
| O4–Mn2–O4 | 95.4(2) | 97.4(3) | 96.6(3) | 98.1(3) | 99.5(3) | 99.1(3) |
| Mn2–O1–Mn2 | 97.5(3) | 98.0(3) | 97.2(4) | 95.2(4) | 95.1(4) | 95.3(4) |
| Mn1–O2–Mn1 | 100.1(4) | 98.98(4) | 98.8(4) | 99.0(5) | 98.3(5) | 96.8(4) |
| Mn1–O3–Mn1 | 93.3(4) | 94.7(4) | 94.8(4) | 94.1(6) | 94.9(6) | 96.6(5) |
| Mn1–O3–Mn2 | 133.2(3) | 132.4(4) | 132.4(4) | 132.5(4) | 131.9(4) | 131.1(4) |
| Mn1–O4–Mn2 | 127.1(3) | 125.6(3) | 125.5(3) | 123.1(4) | 121.8(4) | 122.7(3) |

pyramids, which in fact, form dimer units, $Mn2_2O_8$, as shown in figure 4. The R cations are in the eightfold-oxygen-coordinated holes of the network.

It is noteworthy that $Mn1O_6$ octahedra are fairly flattened, with two bonds significantly shorter than the remaining four Mn–O bonds. For instance, in the La compound Mn1–O3 is 1.881(5) Å, whereas Mn1–O2 and Mn1–O4 are 1.948(4) and 1.932(2) Å, respectively. Similarly flattened octahedra have also been observed in other $Mn^{4+}$-containing structures, such as $\beta$-$MnO_2$ (rutile type) [14], in which the octahedra form infinite chains by edge sharing too. The average ⟨Mn1–O⟩ bond length gradually decreases along the series, as shown in figure 5. $Mn2O_5$ pyramids also show very significantly different bond lengths: four oxygen atoms ($2O1 + 2O4$) are in a square-planar configuration, with Mn–O distances between 1.88 and 1.93 Å, and the fifth oxygen atom is in axial position at a longer distance from Mn, between 2.12 Å (R = La) and 2.02 Å (R = Tb, Ho, Er). Also $Mn2O_5$ and $RO_8$ polyhedra decrease in size from La to Er, scaling with the dimensions of the unit cell.

The observed Mn1–Mn1 distances are extremely short, taking values as small as 2.70 Å for R = Tb, Ho. They are much smaller than the Mn–Mn contact in other comparable phases, such as 2.871 Å in $\beta$-$MnO_2$ [14]. As a consequence of such structural features, the magnetic interactions between manganese cations give rise to complex magnetic behaviours, as described later.

The presence of possible structural stresses in the crystal can be better estimated through the calculation of the valence of the cations and anions present in the solid, by means of the Brown bond valence model [15, 16]. This model gives a phenomenological relationship between the formal valence of a bond and the corresponding bond length. In perfect nonstrained structures the bond valence sum (BVS) rule states that the formal charge of the cation (anion) is equal to the sum of the bond valences around this cation (anion). This rule

is satisfied only if the stress introduced by the coexistence of different structural units can be relieved by the existence of enough degrees of freedom in the crystallographic structure. The departure from the BVS rule is, therefore, a measure of the stress existing in the bonds of the structure.

Table 5 lists the valences calculated for R, Mn and O from the individual R–O and Mn–O distances of table 3. In $LaMn_2O_5$, La cations exhibit a valence significantly larger than that expected of +3; in compensation Mn1 shows a valence lower than +4. Therefore, in the crystal structure La cations are overbonded and Mn1 underbonded, i.e. La–O and Mn1–O bonds are under compressive and tensile stresses, respectively. These structural stresses can be quantified by means of the 'Global instability index' [17], GII in table 5 and

**Table 5.** Valences determined from the bond valence model[a] for R, Mn and O within the $RO_8$, $MnO_6$ and $MnO_5$ coordination polyhedra in $RMn_2O_5$.

| | La | Pr | Nd | Tb | Ho | Er |
|---|---|---|---|---|---|---|
| La | 3.40(1) | 3.36(1) | 3.28(1) | 3.13(1) | 3.08(1) | 3.00(1) |
| Mn1 | 3.83(2) | 3.88(2) | 3.89(2) | 4.02(2) | 4.05(3) | 4.07(2) |
| Mn2 | 3.01(2) | 3.08(2) | 3.14(2) | 3.17(2) | 3.16(2) | 3.20(2) |
| O1 | 2.20(1) | 2.16(1) | 2.21(1) | 2.13(1) | 2.13(2) | 2.12(1) |
| O2 | 2.14(1) | 2.13(2) | 2.10(1) | 1.99(2) | 1.95(2) | 2.02(1) |
| O3 | 1.79(1) | 1.85(2) | 1.89(2) | 2.04(2) | 2.08(2) | 2.00(2) |
| O4 | 2.06(1) | 2.09(1) | 2.06(1) | 2.07(1) | 2.06(1) | 2.07(1) |
| GII | 0.204 | 0.178 | 0.159 | 0.102 | 0.095 | 0.096 |

[a] The valence is the sum of the individual bond valences ($s_i$) for R–O and Mn–O bonds. Bond valences are calculated as $s_i = \exp[(r_0 - r_i)/B]$; $B = 0.37$, $r_0 = 1.760$ for the $Mn^{3+}$–$O^{2-}$ pair, $r_0 = 1.753$ for the $Mn^{4+}$–$O^{2-}$ pair; for the $R^{3+}$–$O^{2-}$ pairs, from La to Er, $r_0 = 2.172, 2.135, 2.117, 2.049, 2.023, 2.010$, from [16]. Individual R–O and Mn–O distances ($r_i$) are taken from table 3. The global instability index (GII) is calculated as the root mean of the valence deviations for the $j = 1, \ldots, N$ atoms in the asymmetric unit, according to $\mathrm{GII} = (\sum_j [\sum_i (s_{ij} - V_j)^2]/N)^{1/2}$.

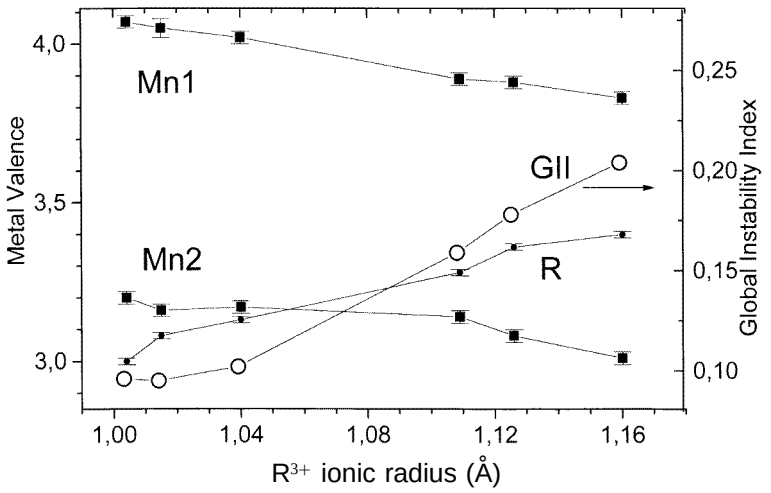


**Figure 6.** Valence of R, Mn1 and Mn2, determined from the Brown [15] model, and global instability index (GII) variation with the rare-earth size.

figure 6, which is calculated from the differences between observed and expected valences for all the atoms in the asymmetric unit. It is a measure of the extent to which the BVS rule is violated over the whole structure. As suggested by Brown [17] and Armbruster *et al* [18], GII values higher than 0.2 vu indicate the presence of intrinsic strains large enough to cause instability at room temperature. This is the case of $LaMn_2O_5$, which in fact is the member of the series that needs more severe preparation conditions [9]. GII values quickly decrease for $RMn_2O_5$ with smaller rare earths, as shown in figure 6, reaching a value of 0.09 for R = Ho, Er. The size of these rare-earth cations seems to be adequate to introduce a minimum of stresses into the crystal structure of this series of materials.

In a previous study by thermal analysis of some members of the series [9], the presence of some oxygen excess in the structure was suggested, which could not be confirmed from XRD data. In the present NPD study, final Fourier synthesis did not yield any identifiable peaks which could indicate additional oxygen atoms in interstitial positions. The presence of oxygen interstitials must be, therefore, excluded.

### *3.2. Magnetic behaviour*

The d.c. magnetic susceptibility of the different members of the $RMn_2O_5$ family is shown in figure 7. Very different behaviour patterns are observed depending on the R cation. The $LaMn_2O_5$ curve presents a clear increase of the magnetization (weak ferromagnetism) below 230 K. At low temperature, there is a very broad maximum (from 20 to 140 K) where a strong dependence on the frequency is observed, as shown in figure 8. The frequency dependence of the real part of the a.c. magnetic susceptibility indicates a spin-glass type behaviour at low temperature, probably related to the weak ferromagnetism. The effective paramagnetic moment for $LaMn_2O_5$, determined at high temperatures, is 6.24 $\mu_B$ per formula unit (table 6). This value is in excellent agreement with that calculated as $\mu = (\mu^2_{Mn^{3+}} + \mu^2_{Mn^{4+}})^{1/2}$, of 6.24 $\mu_B$, taking for $\mu_{Mn^{3+}}$ and $\mu_{Mn^{4+}}$ the spin-only values of 4.90 and 3.87 $\mu_B$, respectively, and confirms the presence of Mn in both oxidation states. However, the magnetic behaviour at lower temperatures, with two types of anomaly, $T_{weak\ ferro} \approx 230$ K and $T_{spin\ glass} \approx 60$ K, is very complicated and deserves a further detailed study. The analysis of low-temperature neutron diffraction data is in progress.

For $PrMn_2O_5$ and $NdMn_2O_5$ a cusp in the susceptibility curve suggests an antiferromagnetic behaviour at low temperatures (25 and 5 K, respectively). This maximum in the magnetic susceptibility is probably related to the transition to a modulated magnetic

**Table 6.** Magnetic constants for $RMn_2O_5$, from magnetic susceptibility data. The paramagnetic moments per formula unit are given in $\mu_B$.

| R | $\mu(R^{3+})$[a] | $\mu_{calc}$[b] | $\mu_{obs}$ | $\theta_p$ (K) |
|---|---|---|---|---|
| L | — | 6.24 | 6.24 | −218 |
| Pr | 3.58 | 7.20 | 7.76 | −102 |
| Nd | 3.62 | 7.22 | 6.85 | −97 |
| Sm | 0.84 | 6.30 | 6.64 | −230 |
| Eu | 0.0 | 6.24 | 7.00 | −135 |
| Tb | 9.72 | 11.55 | 11.05 | −27 |
| Ho | 10.60 | 12.30 | 12.06 | −33 |
| Er | 9.59 | 11.44 | 10.93 | −25 |

[a] Theoretical values for free $R^{3+}$ ions, taken from [19].
[b] $\mu_{calc} = (\mu(R^{3+})^2 + \mu(Mn^{3+})^2 + \mu(Mn^{4+})^2)^{1/2}$.

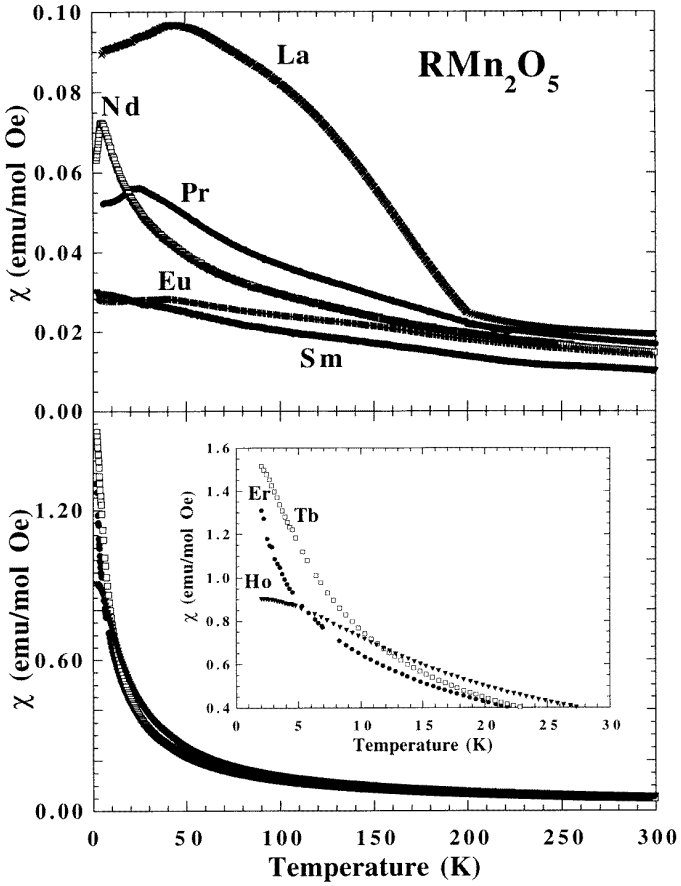


**Figure 7.** Temperature dependence of the d.c. magnetic susceptibility for $RMn_2O_5$ compounds.

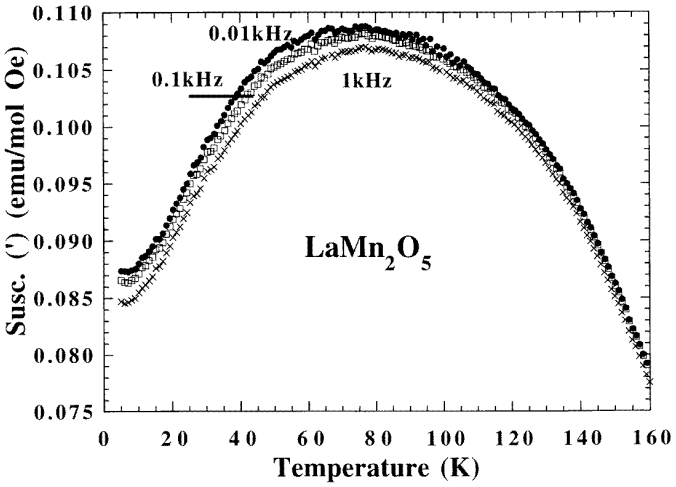


**Figure 8.** Temperature and frequency dependence of the real part of the a.c. magnetic susceptibility for $LaMn_2O_5$.

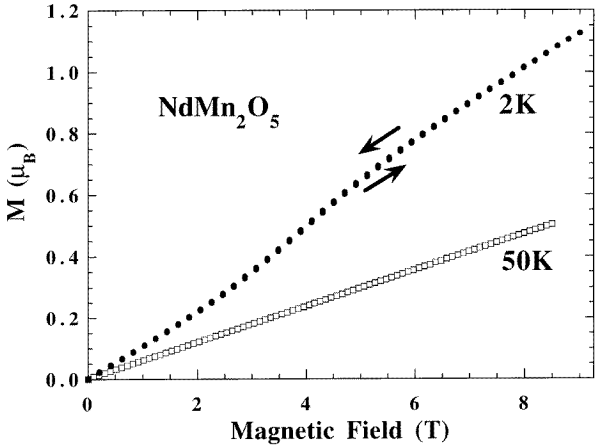


**Figure 9.** Magnetic field dependence of the magnetization for $NdMn_2O_5$, in $\mu_B$ per formula unit.

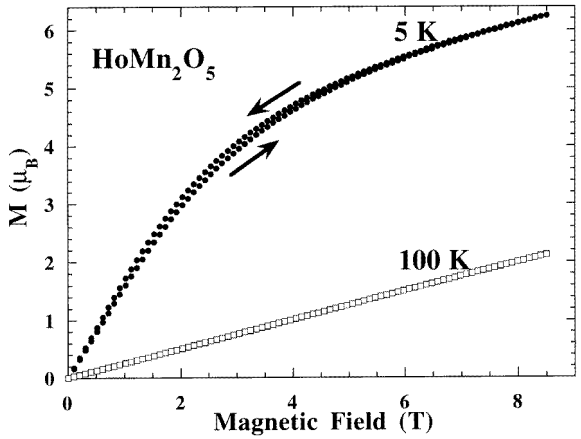


**Figure 10.** Field dependence of the magnetization isotherm for $HoMn_2O_5$.

structure, as observed in different members of this series [6–8]. The magnetization isotherm for $NdMn_2O_5$ (figure 9) shows that the low-temperature magnetic structure undergoes a magnetic-field-induced transition at 2.5 T. The paramagnetic moments per formula unit are 7.76 $\mu_B$ for R = Pr and 6.85 $\mu_B$ for R = Nd, in reasonable agreement with the expected values of 7.20 and 7.22 $\mu_B$, respectively (table 6).

The magnetic susceptibility curves for $SmMn_2O_5$ and $EuMn_2O_5$ below 100 K are dominated by the behaviour of the rare-earth cation. The curves of the terms for the rare earths with higher magnetic moments (R = Tb, Ho, Er), in which the level of the susceptibility is high, show weak anomalies more difficult to analyse (figure 7). A saturation of $\chi$ is observed in the $HoMn_2O_5$ curve below 10 K. In figure 10 the magnetization isotherm for $HoMn_2O_5$ suggests that the low-temperature magnetic ordering is very complex, basically antiferromagnetic with a weak ferromagnetic component (of about 4 $\mu_B$ per formula). The paramagnetic moments determined in the high-temperature region are also in agreement with the expected data (table 6).

## 4. Conclusions

Polycrystalline $RMn_2O_5$ (R = La, Pr, Nd, Tb, Ho, Er) samples have been studied at room temperature by high-resolution neutron diffraction. In the structure, $Mn^{3+}$ and $Mn^{4+}$ occupy different crystallographic positions, a square-pyramidal environment and octahedral coordination, respectively. The sizes of the $Mn^{3+}O_5$, $Mn^{4+}O_6$ and $RO_8$ polyhedra progressively decrease as $R^{3+}$ becomes smaller. A bond valence study shows that $LaMn_2O_5$ contains important stresses in the structure, which are released along the series as the rare-earth cations decrease in size. The magnetic susceptibility for $RMn_2O_5$ at high temperatures is consistent with the presence of high-spin $Mn^{3+}$ and $Mn^{4+}$. For some of the paramagnetic rare-earth compounds there is a magnetic transition at low temperatures to a complex magnetic structure, with field-induced transitions ($NdMn_2O_5$) or showing rather strong ferromagnetic components ($HoMn_2O_5$). Below 230 K, $LaMn_2O_5$ exhibits weak ferromagnetism, and at lower temperatures a spin-glass type behaviour, not observed in the other terms of the series.

## Acknowledgment

The authors acknowledge the financial support of the DGICYT for project PB94-0046.

## References

[1] von Helmholt R, Wecker J, Holzapfel B, Schultz L and Samwer K 1993 *Phys. Rev. Lett.* **71** 2331
[2] Euzen P, Leone Ph, Gueho Ch and Palvadeau P 1993 *Acta Crystallogr.* C **49** 1875
[3] Quezel-Ambrunaz S, Bertaut E F and Buisson G 1964 *C. R. Acad. Sci. Paris* **258** 3025
[4] Bertaut E F, Buisson G, Durif A, Mareschal A, Montmory M C and Quezel-Ambrunaz S 1965 *Bull. Soc. Chim. Fr.* 1132
[5] Abrahams S C and Bernstein J L 1967 *J. Chem. Phys.* **46** 3776
[6] Gardner P P, Wilkinson C, Forsyth J B and Wanklyn B M 1988 *J. Phys. C: Solid State Phys.* **21** 5653
[7] Buisson G 1973 *Phys. Status Solidi* a **17** 191
[8] Wilkinson C, Sinclair F, Gardner P P, Forsyth J B and Wanklyn B M 1981 *J. Phys. C: Solid State Phys.* **14** 1671
[9] Alonso J A, Casais M T, Martínez-Lope M J and Rasines I 1997 *J. Solid State Chem.* **129** 105
[10] Rietveld H M 1969 *J. Appl. Crystallogr.* **2** 65
[11] Rodríguez-Carvajal J 1993 *Physica* B **192** 55
[12] International Centre for Diffraction Data *File Card* 34–667 ($YMn_2O_5$)
[13] Shannon R D 1976 *Acta Crystallogr.* A **32** 751
[14] Bolzan A A, Fong C, Kennedy D J and Howard C J 1993 *Austr. J. Chem.* **46** 939
[15] Brown I D 1981 *Structure and Bonding in Crystals* vol 2, ed M O'Keefe and A Navrotsky (New York: Academic) p 1
[16] Brese N E and O'Keefe M 1991 *Acta Crystallogr.* B **47** 192
[17] Brown I D 1992 *Z. Kristallogr.* **199** 255
[18] Armbuster T, Röthlisberger F and Seifer F 1990 *Am. Mineral.* **75** 847
[19] Kittel C 1976 *Introduction to Solid State Physics* (New York: Wiley)